# RESEARCH ARTICLE

## **PHYSICS**

# An improved bound on the electron's electric dipole moment

Tanya S. Roussy<sup>1,2</sup>†, Luke Caldwell<sup>1,2</sup>†, Trevor Wright<sup>1,2</sup>, William B. Cairncross<sup>1,2</sup>‡, Yuval Shagam<sup>1,2</sup>§, Kia Boon Ng<sup>1,2</sup>, Noah Schlossberger<sup>1,2</sup>, Sun Yool Park<sup>1,2</sup>, Anzhou Wang<sup>1,2</sup>, Jun Ye<sup>1,2</sup>, Eric A. Cornell<sup>1,2</sup>\*

The imbalance of matter and antimatter in our Universe provides compelling motivation to search for undiscovered particles that violate charge-parity symmetry. Interactions with vacuum fluctuations of the fields associated with these new particles will induce an electric dipole moment of the electron (eEDM). We present the most precise measurement yet of the eEDM using electrons confined inside molecular ions, subjected to a huge intramolecular electric field, and evolving coherently for up to 3 seconds. Our result is consistent with zero and improves on the previous best upper bound by a factor of ~2.4. Our results provide constraints on broad classes of new physics above  $10^{13}$  electron volts, beyond the direct reach of the current particle colliders or those likely to be available in the coming decades.

lectric dipole moments of fundamental particles, such as the electron, are signatures of time-reversal symmetry violation, equivalent to violation of combined charge and parity (CP) symmetry (I). CP symmetry is broken in the standard model but only in the quark sector (2), so the coupling to leptons is weak and the predicted electron's electric dipole moment (eEDM) several orders of magnitude below current experimental sensitivity (3, 4). Explaining the imbalance of matter and antimatter in the Universe requires additional CP violation, beyond that present in the Standard Model (5–7). Many proposed

extensions predict new particles at energies higher than any so far discovered, with CP-violating interactions. These new particles can induce a much larger eEDM, often within reach of near-term experiments (8–10). A nonzero measurement at current experimental sensitivities would unambiguously signal new physics, whereas a more precise measurement consistent with zero imposes challenging constraints on possible explanations of the matter-antimatter imbalance. Our measurement uses quantum projection-noise-limited spectroscopy on samples of hundreds of molecular ions with interrogation times of up to

3 s. Our result,  $d_e=(-1.3\pm2.0_{\rm stat}\pm0.6_{\rm sy}]$  Ch up  $10^{-30}~e$  cm, is consistent with zero and  $\epsilon$  an upper bound of  $|d_e|<4.1\times10^{-30}~e$  cm at 90% confidence.

An eEDM  $d_e = d_e \hat{s}$ —with  $\hat{s}$  a unit vector along the spin of the electron-subject to an electric field,  $\mathcal{E}$ , has an energy of  $-d_e \cdot \mathcal{E}$ . The essence of an eEDM search is to measure the energy shift when  $\hat{s}$  is aligned with  $\hat{\mathcal{E}}$  compared with when it is antialigned. The size of the observable shift scales with the size of  $\vec{\mathcal{E}}$ , and thus many existing (11–13) and proposed (14-17) eEDM experiments use electrons embedded inside polar molecules, where intramolecular electric fields can be ~105 times larger than what can be directly applied in the lab. These internal electric fields can be aligned in the lab frame by orienting the molecules with modest external electric fields.

Our measurement uses HfF<sup>+</sup> molecular ions. In an applied electric field of ~58 V cm<sup>-1</sup>, the  $^3\Delta_1$  (v=0,J=1) "science" state of the molecule is split into a series of doublets (Fig. 1A). In two of these doublets, highlighted in color, the molecule is oriented (18); the upper doublet (orange) has the intramolecular axis parallel to the applied field, whereas the lower doublet (blue) is antiparallel. This intramolecular axis defines the direction of an effective

<sup>1</sup>JILA, NIST and University of Colorado, Boulder, CO 80309, USA. <sup>2</sup>Department of Physics, University of Colorado, Boulder, CO 80309, USA.

†These authors contributed equally to this work. ‡Present address: Atom Computing, Berkeley, CA 94710, USA. §Present address: Schulich Faculty of Chemistry, Technion-Israel Institute of Technology, Haifa 3200003, Israel.

\*Corresponding author. Email: cornell@jila.colorado.edu

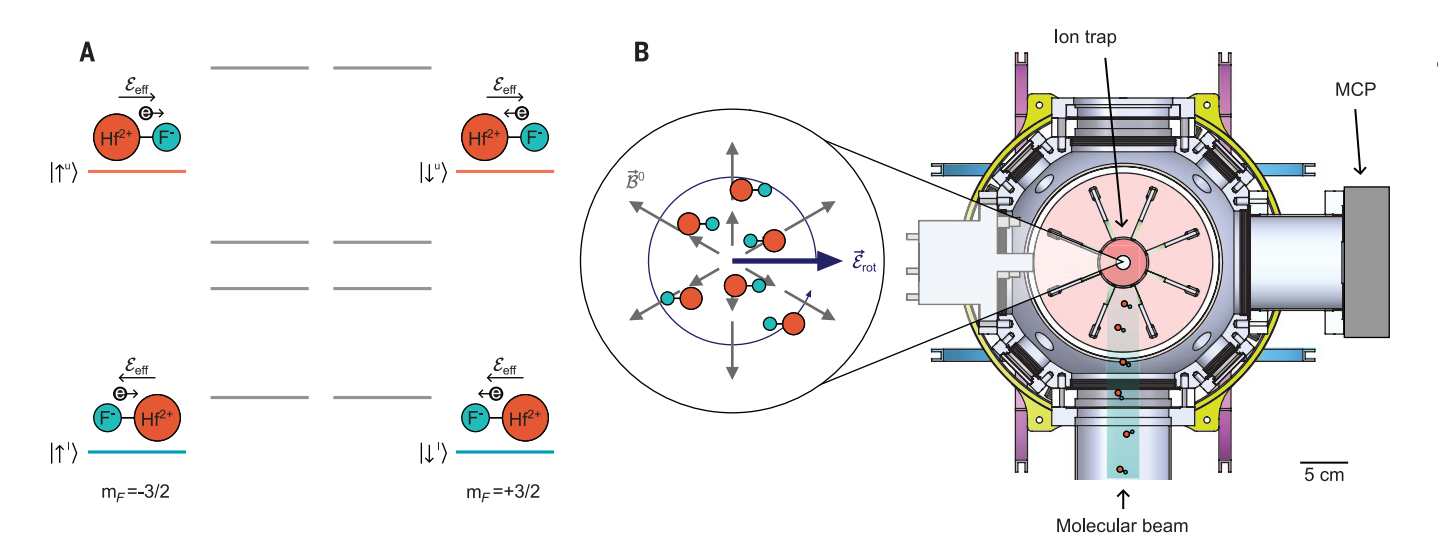


Fig. 1. Experiment outline. (A) Level structure of the eEDM-sensitive  ${}^3\Delta_1$  (v=0,J=1) state. The horizontal axis indicates  $m_F$ , the projection of the total angular momentum onto the externally applied electric field. The vertical axis indicates the energy of the states. The direction of the electron spin and effective electric field,  $\mathcal{E}_{\text{eff}}$ , is indicated for each of the states used in the experiment. (B) Schematic of ion trap, composed of eight radial electrodes and a pair of endcap electrodes. (Inset) Fields applied during experimental sequence: the rotating electric bias field,  $\vec{\mathcal{E}}_{\text{rot}}$ , and the quadrupole magnetic field,  $\vec{\mathcal{B}}^0$ .

electric field,  $\mathcal{E}_{\mathrm{eff}} \approx 23~\mathrm{GV~cm^{-1}}$  (19–22), acting on the spin of one of the valence electrons. In the presence of a small magnetic field, the two states in a doublet correspond to the spin of this valence electron being aligned or antialigned with  $\mathcal{E}_{\mathrm{eff}}$ . We prepare a coherent superposition of the two spin states and measure the energy difference using Ramsey spectroscopy. The eEDM will give a contribution to this energy,  $\pm 2d_e\mathcal{E}_{\mathrm{eff}}$ , with opposite sign in the two doublets. We perform the measurement simultaneously on spatially overlapping clouds of ions prepared in each of the doublets. The difference between the measured energies is our science signal.

# **Experimental overview**

Our experimental apparatus is shown schematically in Fig. 1B. An overview of the experimental sequence is given here; more details, including an account of improvements made since our earlier result (12), are presented in (23, 24). The sequence begins with production and radiofrequency trapping of roughly 20,000 HfF<sup>+</sup> ions. To orient the molecules while maintaining confinement, we rotate the orienting field,  $\vec{\mathcal{E}}_{\rm rot}$ , at angular frequency  $\omega_{\rm rot} = 2\pi \times 375$  kHz and perform our spectroscopy in this rotating frame. We also apply a quadrupole magnetic field gradient,  $\vec{\mathcal{B}}^0$ , to create a time-averaged effective bias magnetic field,  $\mathcal{B}_{\rm rot}$  (24).

We prepare an incoherent mixture of one of the spin states from each doublet, either  $|\!\!\uparrow^u\rangle$  and  $|\!\!\uparrow^l\rangle$  or  $|\!\!\downarrow^u\rangle$  and  $|\!\!\downarrow^l\rangle$  (Fig. 1A), and then apply a  $\frac{\pi}{2}$  pulse to create a coherent superposition of the two states in each doublet. We allow the superpositions to evolve for a variable amount of time, then apply a second  $\frac{\pi}{2}$  pulse to map the accumulated relative phase between the states in a doublet onto a population difference between those states. We clean out the population in one of

the spin states in each doublet, either  $|\uparrow^{\mathrm{u}/l}\rangle$  or  $|\downarrow^{\mathrm{u}/l}\rangle$ , then count the number of ions in the remaining stretched states by state-selectively photodissociating the molecules and detecting the resultant Hf<sup>+</sup> ions (25). We use the opposing orientations of the two doublets in the trap to send the Hf<sup>+</sup> ions originating from molecules in each doublet to opposite sides of our imaging microchannel plate (MCP) and phosphor screen assembly (26, 27). We then repeat the procedure with the opposite initial

**Table 1. Summary of systematic shifts and their uncertainties.** Data are as presented in (23). All values are in microhertz.

Effect	Correction	Uncertainty
Magnetic		
Nonreversing $\vec{\mathcal{B}}^0$	0.1	< 0.1
Stray ${\cal B}$ fields + distortion of ${\cal E}_{\sf rot}$		3.2
Berry's phase		
Rotation-odd axial secular motion		3.4
Axial fields at harmonics of $\mathcal{E}_{rot}$		3.4
Simultaneous doublet spectroscopy		
Imperfect spatial overlap		3.5
Imperfect imaging contrast		1.4
Other		
Rotation-induced m <sub>F</sub> -level mixing		0.4
Total	0.1	6.9

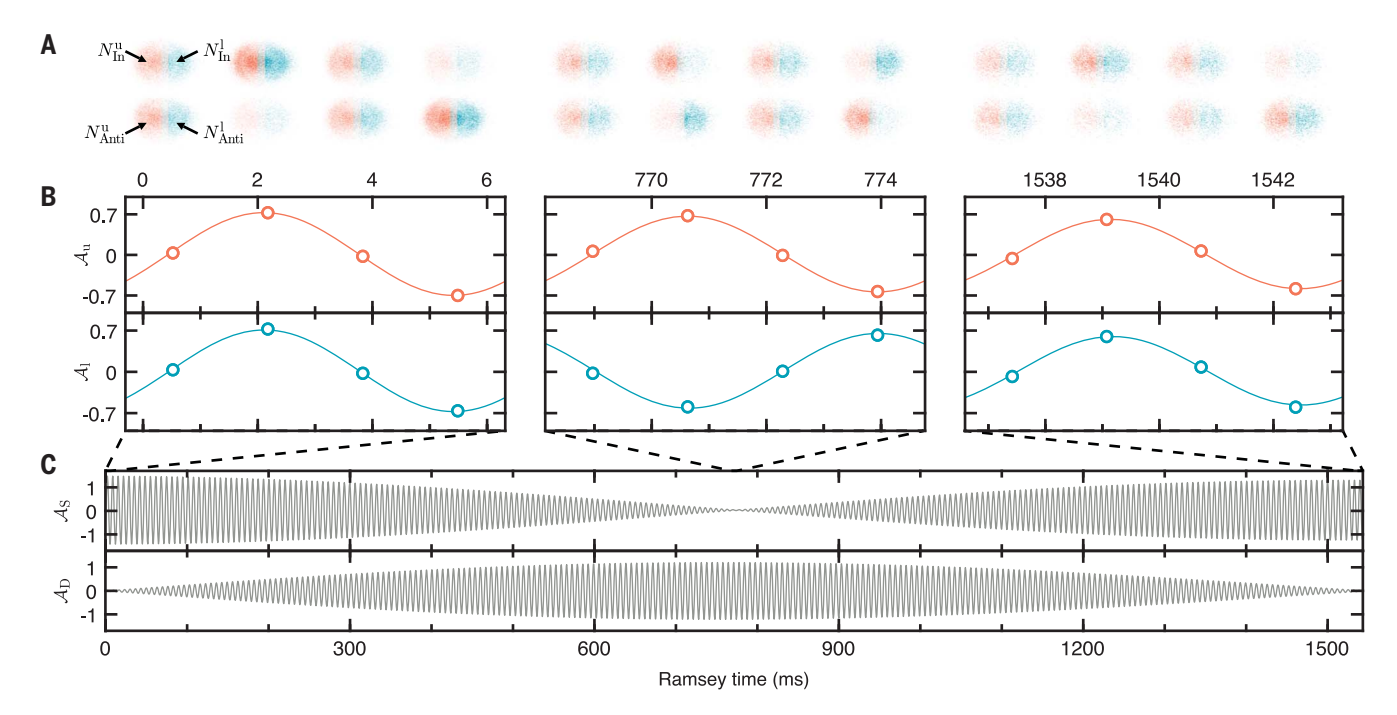


**Fig. 2. Example Ramsey data.** (**A**) Detection of Hf<sup>+</sup> ions; ions are assigned to the upper or lower doublet based on their position (upper doublet shown in orange, lower doublet in blue). Counts from a thin central swatch where the assignment is ambiguous (shown in gray) are removed. Images shown are averaged over 60 shots of the experiment. (**B**) Asymmetries for the upper and lower doublet. (**C**) Fitted sum and difference asymmetries,  $A_S$  and  $A_D$ , used to extract mean and difference frequencies,  $f_m$  and  $f_d$ . Middle-time data, where the two doublets are out of phase, were collected in this example dataset for illustrative purposes only. Such data contribute very little to the frequency determination and were not collected during the final precision dataset.

spin state. Example data are shown in Fig. 2A. We count the ions on each side of the screen, in each configuration—typically ~120 ions from each doublet after a 3-s hold time—and from these two measurements construct the two asymmetries,  $\mathcal{A}_u$  and  $\mathcal{A}_l$ , where

$$\mathcal{A}_{\text{u/l}} = \frac{N_{\text{In}}^{\text{u/l}} - N_{\text{Anti}}^{\text{u/l}}}{N_{\text{In}}^{\text{u/l}} + N_{\text{Anti}}^{\text{u/l}}} \tag{1}$$

Here,  $N_{\rm In}^{\rm u/l}$  and  $N_{\rm Anti}^{\rm u/l}$  are the number of ions counted, u/l indicates the upper or lower doublet, and the subscripts indicate whether we read out the same state that we prepare (In) or the opposite (Anti). We repeat our measurement at different free-evolution times, generating a pair of Ramsey fringes as shown in Fig. 2B. The frequencies of these two fringes are proportional to the energy splitting in the two doublets. The primary contribution to this energy splitting is the Zeeman splitting,  $3g_F\mu_B\mathcal{B}_{\rm rot}$ , where  $g_F=-0.0031(1)$  is the g factor of the science state (28). For our typical experimental parameters, this produces fringe frequencies of ~100Hz. Other effects, including the eEDM, make small modifications to this frequency.

Instability of the intensity of the pulsed lasers used for creation and photodissociation of the ions (24) creates considerable noise in the number of ions measured in each shot of the experiment, typically approximately three times as large as the quantum projection—

noise limit on the side of the fringe at 3 s. However, these sources of noise, and many others, are common mode between the two doublets—the exact same laser pulses address both clouds of ions—and so the noise in  $\mathcal{A}_u$  and  $A_l$  is highly correlated. To take advantage of this, we form the sum and difference asymmetries  $A_S = A_u + A_l$  and  $A_D = A_u - A_l$  (Fig. 2C). If we take data when the two doublets are close to being in phase, the noise in  $A_D$  is drastically reduced (27). The two doublets oscillate at slightly different frequencies,  $f_{\rm u}$ and  $f_1$ , owing to a ~1/230 fractional difference in their magnetic moments, and so during the eEDM dataset we deliberately take our data at a beat. We take two sets of points: the early-time data, when the two doublets are in phase, and the late-time data ~230 oscillations later, when they come back into phase again. We can control the time of the second beat by varying the strength of the magnetic bias field,  $\mathcal{B}_{rot}$ . We fit to  $\mathcal{A}_{S}$  and  $\mathcal{A}_{D}$  to extract the mean of the two fringe frequencies,  $f_{\rm m}=$  $\frac{1}{2}(f_{\rm u}+f_{\rm l})$ , and their difference,  $f_{\rm d}=\frac{1}{2}(f_{\rm u}-f_{\rm l})$ .

We collect Ramsey fringes in  $2^3=8$  experimental states, corresponding to each possible combination of three binary experimental switches,  $\{\tilde{B},\tilde{R},\tilde{I}\}=\pm 1$ .  $\tilde{B}$  is the direction of the magnetic bias field relative to  $\vec{\mathcal{E}}_{\rm rot}$ ,  $\tilde{R}$  the rotation direction of  $\vec{\mathcal{E}}_{\rm rot}$ , and  $\tilde{I}$  the direction of  $\vec{\mathcal{E}}_{\rm rot}$  relative to the imaging MCP at the instant of photodissociation, determining which side

of the phosphor screen each of the doublets is imaged onto. A set of Ramsey fringes in each of the 8 switch states forms a block. To minimize the effects of experimental drifts, within a block we interleave data collection for the switch states; the first Ramsey time is recorded for all switch states before moving onto the second Ramsey time for each switch state, and so on. We take the 16 fitted frequencies from each block and form 16 linear combinations to give the components of the measured frequencies. which are even or odd under each of the experimental switches. Following (29), we label the components with superscripts that denote the switches under which the quantity is odd. For example, our science signal is  $f^{DB}$ , the component of the difference frequency that is odd under  $\tilde{B}$  but even under  $\tilde{R}$  and  $\tilde{I}$  (30). The other channels allow us to diagnose systematics and monitor experimental performance.

Over the course of the dataset, we varied a number of other experimental parameters on timescales slower than a block. These include the state we read out at the end of the Ramsev sequence, denoted  $\tilde{P}=\pm 1$  and alternated each block; the order in which the switch states are recorded at each Ramsey time, alternated every other block; three different magnitudes of the magnetic bias field, corresponding to mean fringe frequencies of  $f^0 \sim 77$ , 105, and 151 Hz; and reversal of the waveplates that set the lab-frame handedness of the light used for state preparation and readout. During data collection and analysis, we "blinded" our measurement of  $f^{DB}$  by adding an unknown offset to this channel. The offset was not removed until our systematics search and analysis (23) were complete.

# **Accuracy evaluation**

To evaluate the accuracy of our measurement, we searched extensively for systematic shifts before data collection; a summary is given in Table 1. In general, we tuned a variety of experimental parameters over ranges that were large compared with those present during data collection, exaggerating any accompanying systematic effects, and observed the response in our data channels. The only shift we could observe directly in the eEDM channel stems from a nonreversing quadrupole magnetic field and the difference in magnetic moments between the two doublets, caused primarily by the applied electric field mixing the states of the two doublets with higher rotational levels of the molecule. The  $f^B$  channel provides a direct measurement of the nonreversing magnetic field and allows us to apply a correction to our science channel,  $\delta f_{\text{corr}}^{DB} =$  $f^B \frac{\delta g_F}{g_F}$ , where  $\delta g_F$  is half the difference between the g factors for the upper and lower doublets (Fig. 3A). Before applying any corrections to the science channel, we suppress this systematic by actively shimming the currents through

the measurement. (A) Shift in fDB caused by nonreversing magnetic quadrupole field, which can be corrected by using the shift in the  $f^B$ channel, which is ~460 times as large as the  $f^{DB}$ shift. (**B**) Shift in the  $f^B$  channel caused by deliberately applied secondharmonic electric field  $\mathcal{E}_{2h}$  with transverse magnetic field, B. Data show variation in shift as angle  $\theta_{2h}$  between  $\mathcal{E}_{2h}$  and x axis is varied.  $\mathcal{E}_{2h}$  is ~250 times as large as that present in the experiment;  $\mathcal{B}$  is ~ 14 mG. (Inset) Lissajous figure traced out by total electric field for greatly exaggerated ratio of  $\mathcal{E}_{2h}/\mathcal{E}_{rot}$ ; blue and orange show one-half

cycle each. The field points in

the -x direction for more time

than in the +x direction.

Fig. 3. Systematic shifts in

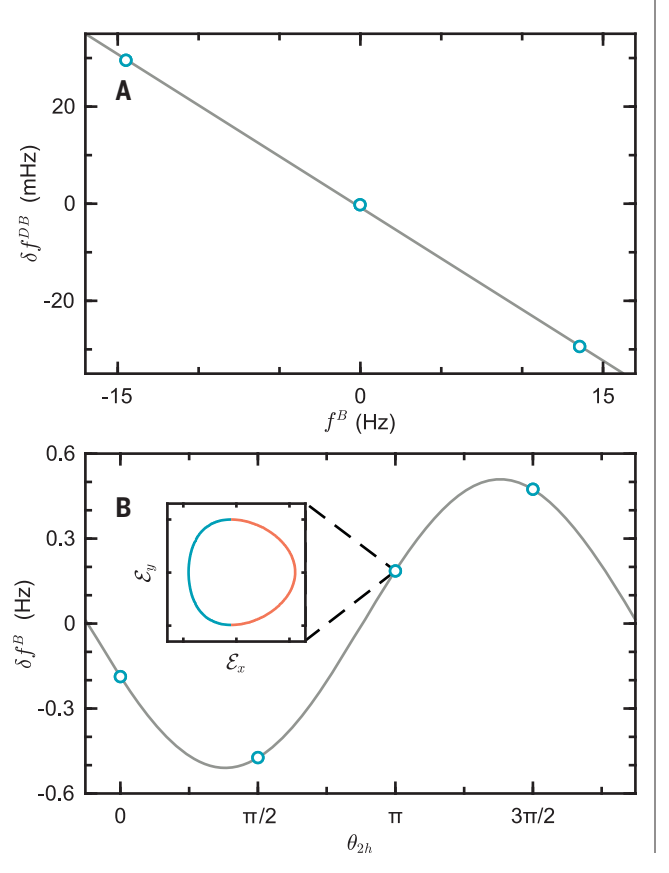
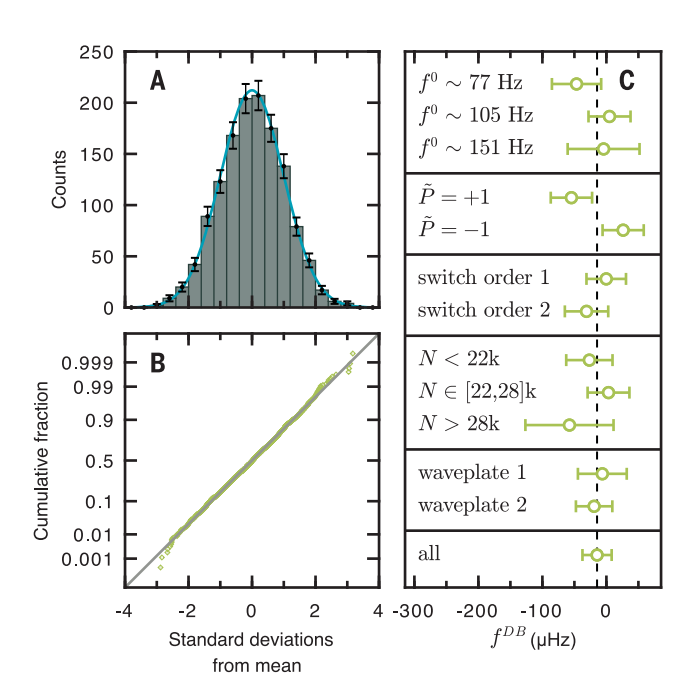


Fig. 4. Summary of our dataset. Cuts have been applied and the uncertainty on each block scaled by  $\sqrt{\chi^2}$  to account for overscatter. (A) Histogram of data. Error bars show standard deviation of bin counts expected from Poisson distribution. The blue line shows normal distribution. (B) Normal probability plot of  $f^{DB}$ . showing that the data are consistent with a normal distribution. The gray line shows expected probability for a normal distribution. (C) Variation of central value under different experimental parameters compared with the overall average value of  $f^{DB}$ . Here. N is the



average number of trapped HfF<sup>+</sup> ions per experimental trial during a block. Other panels in (C) are described in the final paragraph of the Experimental Overview section.

the coils that apply the magnetic bias field to minimize  $f^B$ . This shimming was so effective that the mean correction that we applied was well below our statistical sensitivity,  $\delta f_{\rm corr}^{DB} = 90 \text{ nHz.}$ 

The shimming and correction procedure leaves us susceptible to other possible effects that cause shifts in  $f^B$  and  $f^{DB}$  with a ratio different from  $\frac{\delta g_F}{g_F}$ . An important example of such a shift is the combination of a transverse magnetic field with an electric field oscillating at  $2\omega_{rot}$ , which was present in our experiment owing to harmonic distortion in the amplifiers driving the trap electrodes. The harmonic distortion causes the electric field, and thus the magnetic moment of the molecule, to spend more time pointing in one spatial direction than the other, giving a nonzero time-averaged Zeeman interaction with a background magnetic field. This causes shifts in  $f^B$  but no corresponding shifts in  $f^{DB}$ , where the effect is canceled by the coincident change in the size of the differential magnetic moment owing to the distortion. Figure 3B shows the shift in  $f^B$  when we deliberately apply a secondharmonic electric field and vary its angle. We shim out the second harmonic on each electrode by feeding forward a second-harmonic signal with the opposite phase, suppressing the amplitude by ~80 dB. We used magnetic shim coils to null the ambient magnetic field at the trap center to <10 mG. The measured sizes of the residual effects were used to compute the maximum size of the systematic during our dataset.

A full account of all systematic shifts considered is presented in (23).

# Measuring the eEDM

We collected 1370 blocks over about 2 months, corresponding to ~620 hours of data and ~108 ion detection events. Each block results in one value of  $f^{DB}$  and thus a single measurement of  $d_e$ . The uncertainty on  $f^{DB}$  for each block is calculated with only the standard errors on the asymmetries for that block. We applied cuts to the blinded data on the basis of non-eEDM channels that indicated signal quality. Blocks with late-time contrast < 0.2 were cut because of a low signal-to-noise ratio, as were blocks containing fitted fringe frequencies that were >3.5σ different from the mean fringe frequency for that switch state. After applying cuts, we were left with 1329 blocks with  $\chi^2=1.07(4)$ for  $f^{DB}$ . Figure 4, A and B, show the distribution of measured  $f^{DB}$  values over the 1329 blocks after relaxing the uncertainty for each of the blocks by a factor of  $\sqrt{\chi^2} = 1.035$ . The data are consistent with a normal distribution. Our final statistical uncertainty of 22.8 uHz is obtained with these relaxed uncertainties. Based on the number of ions detected in each shot, this uncertainty is ~30% above the quantum projection-noise limit. More details on how we determine uncertainties are given in (24).

Figure 4C shows how the measured value of  $f^{DB}$  depends on experimental parameters varied during the dataset; we find no concerning dependencies.

We removed our blind on 1 November 2022, and obtained a final value for the eEDMsensitive frequency channel

$$f^{DB} = -14.6 \pm 22.8_{
m stat} \pm 6.9_{
m syst} \ \mu 
m Hz \ \ \ \ (2)$$

Dividing by  $-2\mathcal{E}_{\mathrm{eff}}\frac{\mathrm{sgn}(g_F)}{\hbar}\simeq 1.11\times 10^{31}~\mu\mathrm{Hz}$   $e^{-1}~\mathrm{cm}^{-1}~(2I,3I)$ , we obtain a value for the eEDM

$$d_e = (-1.3 \pm 2.0_{\text{stat}} \pm 0.6_{\text{syst}}) \times 10^{-30} \ e \ \text{cm} \ (3)$$

which is consistent with zero within one standard error. The combined statistical and systematic uncertainty,  $\sigma_{d_e} = 2.1 \times 10^{-30} e \text{ cm}$ , improves on our previous work (12) by a factor of ~37, and on the previous state-of-the-art from the ACME collaboration (13) by a factor of ~2. This result and that of the ACME collaboration-two measurements using very different experimental platforms with contrasting sources of systematic shifts-are consistent at slightly above one standard error.

#### Discussion

We use our result to obtain an upper bound using a folded Gaussian distribution

$$|d_e| < 4.1 imes 10^{-30} \ e \ {
m cm} \ \ (90\% \ \ {
m confidence})$$

This limit constrains extensions to the Standard Model that predict new sources of CP-symmetry violation to explain the matterantimatter asymmetry of the Universe (32). Many extensions, including supersymmetry, the two-Higgs model, and left-right symmetric models, generate an eEDM at the one-loop level (33), with magnitude (9)

$$d_e \sim \frac{ea_0\alpha}{2} \frac{g^2}{2\pi} \sin \phi_{\rm CP} \frac{m_e^2}{M^2} \tag{5}$$

Here, M is the characteristic mass of new particles with effective coupling strength, g, to the electron;  $\phi_{\text{CP}}$  is the phase that describes how strongly the interaction violates CP symmetry;  $m_e$  and e are the mass and charge of the electron respectively; and  $\alpha$  is the fine-structure constant. Because  $d_e \propto M^{-2}$ , and because our limit in Eq. 4 is a factor of ~2.4 smaller than the limit reported in (13), we are sensitive to new particles with mass that is  $\sqrt{2.4} = 1.5$  times as large.

To estimate the mass reach of our experiment, we need to make assumptions for the size of  $g^2$  and  $\sin\phi_{CP}$ . For the strong force, quantum electrodynamics, and the weak force,  $g^2 \approx 1, 1/137$ , and  $10^{-6}$ , respectively. For extensions to the Standard Model seeking to explain the matter-antimatter asymmetry, the naive expectation is that  $\sin \phi_{CP} \sim 1$ . With this assumption, we can interpret our new limit on  $d_e$  as  $M \gtrsim (g/\alpha^{\frac{1}{2}})$  40 TeV. For new particles with  $g^2$ of order  $\alpha \sim 1/137$ , this bound is an order of magnitude greater than the largest-mass particles that can be directly detected at the Large Hadron Collider (34).

So far, we have assumed that CP violation arises purely from  $d_e$ . Diatomic molecules are also sensitive to pseudoscalar-scalar electron-nucleon coupling,  $C_S$  (35, 36), and we can interpret our measurement as a linear combination,  $hf^{DB} \times \mathrm{sgn}(g_F) = -2\mathcal{E}_{\mathrm{eff}}d_e + 2W_SC_S$ , where  $\frac{W_S}{h} = -51$  kHz (31) is a molecule-specific structure constant. Assuming that  $d_e$  is zero, we can instead attribute our measurement to  $C_S$ , and we find

$$C_S = (-1.4 \pm 2.2_{\text{stat}} \pm 0.7_{\text{syst}}) \times 10^{-10}$$
 (6)

Determining rigorous limits on  $d_e$  and  $C_S$  requires combining the results of two or more measurements using molecules with different ratios of  $\mathcal{E}_{\rm eff}$  to  $W_S$ . Figure S1 shows a combined fit to the results of this work and (13), giving upper bounds of  $|d_e| < 2.1 \times 10^{-29} \ e\,{\rm cm}$  and  $|C_S| < 1.9 \times 10^{-9}$  with 90% confidence. Our measurement improves these bounds by factors of 16 and 12, respectively (37).

#### **REFERENCES AND NOTES**

- I. B. Khriplovich, S. K. Lamoreaux, CP Violation Without Strangeness: Electric Dipole Moments of Particles, Atoms, and Molecules, Texts and Monographs in Physics (Springer, 1997).
- 2. C. Patrignani, Chin. Phys. C 40, 100001 (2016).
- Y. Yamaguchi, N. Yamanaka, Phys. Rev. Lett. 125, 241802 (2020)
- Y. Ema, T. Gao, M. Pospelov, Phys. Rev. Lett. 129, 231801 (2022).
- M. Dine, A. Kusenko, Rev. Mod. Phys. 76, 1–30 (2003).
- 6. A. D. Sakharov, *Pis'ma Z. Eksp. Teor. Fiz.* **5**, 32–35 (1967).

- M. B. Gavela, P. Hernández, J. Orloff, O. Pène, *Mod. Phys. Lett.* A 09, 795–809 (1994).
- 8. M. Pospelov, A. Ritz, Ann. Phys. 318, 119-169 (2005).
- J. Engel, M. J. Ramsey-Musolf, U. Van Kolck, Prog. Part. Nucl. Phys. 71, 21–74 (2013).
- 10. Y. Nakai, M. Reece, J. High Energy Phys. 2017, 31 (2017).
- 11. J. J. Hudson et al., Nature 473, 493-496 (2011).
- 12. W. B. Cairncross et al., Phys. Rev. Lett. 119, 153001 (2017).
- ACME Collaboration, *Nature* **562**, 355–360 (2018).
   I. Kozyryev, N. R. Hutzler, *Phys. Rev. Lett.* **119**, 133002
- (2017).
   A. Vutha, M. Horbatsch, E. Hessels, *Phys. Rev. A* 98, 032513
- (2018).

  16. The NL-eEDM collaboration et al., Eur. Phys. J. D 72, 197
- (2018). 17. N. Fitch, J. Lim, E. Hinds, B. Sauer, M. Tarbutt, *Quantum*
- Sci. Technol. **6**, 014006 (2020). 18. A. E. Leanhardt et al., J. Mol. Spectrosc. **270**, 1–25 (2011).
- E. R. Meyer, J. L. Bohn, M. P. Deskevich, *Phys. Rev. A* 73, 062108 (2006).
- A. Petrov, N. Mosyagin, T. Isaev, A. Titov, *Phys. Rev. A* 76, 030501 (2007).
- 21. L. V. Skripnikov, J. Chem. Phys. 147, 021101 (2017).
- 22. T. Fleig, Phys. Rev. A 96, 040502 (2017).
- L. Caldwell et al., Systematic and statistical uncertainty evaluation of the HfF+ electron electric dipole moment experiment. arXiv:2212.11837 [physics.atom-ph] (2022).
- Materials and methods are available as supplementary materials.
- 25. K. K. Ni et al., J. Mol. Spectrosc. **300**, 12–15 (2014).
- 26. Y. Shagam et al., J. Mol. Spectrosc. 368, 111257 (2020)
- Y. Zhou et al., Phys. Rev. Lett. 124, 053201 (2020).
   H. Loh, "Search for an electron electric dipole moment with trapped molecular ions," thesis, University of Colorado Boulder
- and JILA (2013). 29. J. Baron et al., Science **343**, 269–272 (2014).
- 30. We define the mean frequency to be always positive. If we had instead allowed the fringe frequency to change sign when the sign of the magnetic bias field changes, our science signal would have been f<sup>0</sup>.
- 31. T. Fleig, M. Jung, J. High Energy Phys. 2018, 12 (2018).
- L. Canetti, M. Drewes, M. Shaposhnikov, New J. Phys. 14, 095012 (2012).

- 33. T. Chupp, P. Fierlinger, M. Ramsey-Musolf, J. Singh, *Rev. Mod. Phys.* **91**, 015001 (2019).
- 34. T. Bose et al. in Proceedings of the 2022 Snowmass Summer Study, Seattle, WA, 17 to 26 July 2022.
- T. Chupp, M. Ramsey-Musolf, Phys. Rev. C Nucl. Phys. 91, 035502 (2015).
- 36. M. Denis et al., New J. Phys. 17, 043005 (2015).
- Improvements are given with respect to equivalent bounds calculated from combined fit to results of (13) and (12).
- T. S. Roussy et al., Data presented in "An improved bound on the electron's electric dipole moment," Zenodo (2023); https://doi.org/10.5281/zenodo.7837398.

## **ACKNOWLEDGMENTS**

We thank the staff at JILA for making this experiment possible. Funding: This work was supported by the Cydney and Tom Marsico Family Foundation, the Sloan Foundation, the Gordon and Betty Moore Foundation, NIST, and the NSF (award PHY-1125844). T.W. acknowledges funding support from NSF GRFP. Author contributions: All authors contributed, in varying degrees, to the conception of experimental approach, molecular survey spectroscopy, apparatus design and construction, apparatus debugging and commissioning, apparatus maintenance, data collection and analysis, analysis of systematic errors, and preparation of publications. We are all responsible for the accuracy of the bottom-line result and of the written account we have submitted to Science. Competing interests: The authors declare that they have no competing interests. Data and materials availability: Data and code used for analysis are available at Zenodo (38). License information: Copyright © 2023 the authors, some rights reserved; exclusive licensee American Association for the Advancement of Science. No claim to original US government works, https://www.science.org/about/sciencelicenses-journal-article-reuse

#### SUPPLEMENTARY MATERIALS

science.org/doi/10.1126/science.adg4084 Materials and Methods Figs. S1 and S2 References (39–42)

Submitted 22 December 2022; accepted 18 May 2023 10.1126/science.adg4084